Role of the Low-Frequency Deformation Field on the Explosive Growth of Extratropical Cyclones at the Jet Exit. Part I: Barotropic Critical Region

G. RIVIÈRE AND A. JOLY

Centre National de Recherches Météorologiques, Météo-France, Toulouse, France

(Manuscript received 24 November 2004, in final form 7 December 2005)

ABSTRACT

By using new theoretical results on perturbation growth in spatially and temporally complex quasigeostrophic flows, this paper investigates the role of the large-scale deformation field on extratropical cyclones and especially on their explosive growth in the jet-exit region. Theoretical ideas are tested by decomposing the atmospheric flow into a high- and a low-frequency part and by analyzing four-dimensional variational data assimilation (4DVAR) reanalysis data of the Fronts and Atlantic Storm-Track Experiment (FASTEX) during February 1997 as well as reanalysis data for the end of December 1999.

Regions where the low-frequency deformation magnitude is greater than the absolute value of the low-frequency vorticity are shown to correspond to regions where synoptic disturbances at the same level tend to be located. These regions in the upper troposphere are intrinsically related to the horizontal inhomogeneities of the low-frequency large-scale upper-tropospheric jet but cannot be detected by looking separately at the deformation or vorticity. Transitions from one such large-scale region to the next furthermore can be accompanied by a sudden change of the dilatation axes orientation: this combination defines a barotropic critical region (BtCR). Reasons why a BtCR is a specific place where barotropic development is likely to occur are exposed. Two very differently located BtCR regions in two apparently similar zonal-like weather regimes are shown to be the preferred regions where synoptic eddies tend to cross the jet from the south to the north.

BtCRs are also special regions where constructive association between barotropic and baroclinic processes is favored, indeed constrained to cooperate. This is illustrated through the detailed analysis of the last growth stage of Intensive Observation Period 17 (IOP17) of FASTEX. It happens precisely around a BtCR area located in the jet-exit region. Two processes explain this IOP17 development; one involves the barotropic generation rate resulting from the low crossing the BtCR and the other one is baroclinic interaction, which is strongly maintained far away from the baroclinicity maximum because of the new favorable baroclinic configuration resulting from the first process.

1. Introduction

Many observations have illustrated how the large-scale flow related to the jet streams plays a crucial role on the shape, growth, and trajectories of midlatitude cyclones (Evans et al. 1994; Young 1995; Schultz et al. 1998; Ayrault 1998; among others) and more generally of all transient synoptic eddies at different levels (e.g., Lau 1988; Sickmoller et al. 2000). While the jet stream baroclinicity is the main source of energy for synoptic eddy growth, numerous numerical studies have shown that the horizontal inhomogeneities of the jet, or in other words the large-scale barotropic deformation field, modulate synoptic eddies growth rates and their location. Studies from Hoskins and West (1979), Simmons and Hoskins (1980), James (1987), Davies et al. (1991), and Barcilon and Bishop (1998) exhibited this result in zonal sheared flows while the works of Shutts (1983), Pierrehumbert (1984), Cai and Mak (1990), Whitaker and Barcilon (1992), and Bishop (1993) presented it in zonally varying or confluent/diffluent flows. Thorncroft et al. (1993) showed also that introducing an asymmetry between the cyclonic and anticyclonic parts of the zonal jet leads to very different baroclinic eddy life cycles. All these idealized studies have proved the impact of the different parts of the barotropic deformation field on baroclinic eddy development and their

Corresponding author address: Dr. G. Rivière, Météo-France, CNRM/GMAP/RECYF, 42 av. G. Coriolis, 31057 Toulouse CEDEX, France.
E-mail: gwendal.riviere@cnrm.meteo.fr

potentially equal importance; but, because of the complexity of the real jet stream deformation field, its different components have been usually studied separately.

Mak and Cai (1989) offered a simple understanding of the simultaneous action of the stretching and shearing terms without making any assumption on their form by introducing the deformation vector (the **D** vector) and showing its implication in the barotropic generation term. This simple mathematical formulation is an easy way to study the role of the large-scale deformation on individual cyclone development and has allowed some authors to reveal the non negligible role played by the barotropic interaction in some real cases (Lackmann et al. 1999; Kucharski and Thorpe 2000). However, recently, Rivière et al. (2003, 2004, hereafter RHK03 and RHK04), demonstrated in a quasigeostrophic context that the deformation field action cannot be understood by looking only at the **D** vector, as the deformation field has also a rotational component which is reduced to the relative vorticity in its simplest form. Even if this rotational component is not involved directly in the energy equations, it first acts on the shape of the perturbation (or eddy) and indirectly on the barotropic and baroclinic conversion terms. The aim of the present paper is to interpret the role of the large-scale deformation field on the evolution of observed midlatitude cyclones by using some results developed in RHK03 and RHK04 that take into account the whole deformation tensor and not only a part of it. It will be shown especially that regions where the deformation field is most active do not correspond to large values of the **D** vector modulus but to large values of a diagnostic parameter involving the stretching and shearing terms and the vorticity of the large-scale flow; that is, all the horizontal derivatives of the horizontal large-scale wind.

All the previous cyclone studies on the role of the large-scale deformation were focused either on the initiation stages of surface cyclones or on the development of upper-level precursors. Lackmann et al. (1999) and Kucharski and Thorpe (2000) showed how the deformation can create upper disturbances via barotropic generation terms while Mallet et al. (1999a) and Chaboureau and Thorpe (1999) validated the theory proposed by Bishop et Thorpe (1994) on the initiation of new cyclones from frontal wave development. Our study has to be contrasted with those previously cited as it involves the large-scale deformation in mature stages of cyclones; that is, cyclones that are not in their initiation stage and it focuses in particular on those that strongly deepen at the exit of the large-scale upper-level jet.

One of the main results of the Fronts and Atlantic Storm-Track Experiment (FASTEX; Joly et al. 1999) described in Baehr et al. (1999) was that strong deepening rates of cyclones occurred in the eastern Atlantic in a region where the large-scale upper-level flow is diffluent. Another essential ingredient revealed by this paper is the recurrent crossing of the jet stream from the warm to the cold-air side to get rapid cyclone intensification during the FASTEX period. Baehr et al. emphasized the fact that these strong deepening rates by crossing the jet occur with or without the presence of a jet streak. The background conditions for rapid cyclone intensification are thus more related to the large-scale flow and occur when the cyclone crosses the large-scale upper-level jet in its region of diffluence. Strong cyclone development in the eastern Atlantic seems not to be a specific characterization of the FASTEX period as shown for example in Young (1995). Furthermore, strong explosive cyclone growth can occur in the Atlantic jet-exit region to form devastating wind storms in Europe as was the case during the Christmas storms of 1999.

One question that rises naturally from the discussion of the previous paragraph is: how and why do cyclones strongly develop in the diffluent part of the jet by crossing it from the warm to the cold-air side in a region where the environmental baroclinicity is not the largest? This could be explained and seems to be commonly understood by the analogy with jet streaks theory; as a jet streak induces surface cyclogenesis in its left-exit region due to divergence processes associated with ageostrophic winds in the upper levels (Uccellini 1990), in the same manner cyclones strongly grow in the left-exit region of the large-scale jet stream. It is, however, difficult to rationalize the dynamical processes involved by doing this parallel between jet streaks and jet streams as the former concerns the total field; that is, has a high- and a low-frequency part whereas the latter is only a low-frequency quantity. In other words, it is not clear that a low-frequency divergence will strengthen the surface cyclone. Moreover, note that the relevance of a diffluent region is not generally accepted (Sanders 1993) and other ingredients could be important to explain the previously mentioned observational evidences of cyclone growth at the jet exit.

Another argument to explain strong cyclone growth at the jet exit far away from the baroclinicity maximum is to invoke downstream development processes described by Orlanski and Katzfey (1991) and Orlanski and Sheldon (1995). The authors presented evidences from case studies analysis that a cyclone can grow by retrieving energy via ageostrophic geopotential fluxes

from another cyclone located upstream, which itself grows by extracting energy baroclinically from the mean flow. These processes need more than one synoptic system to occur but some well-known storms developing at the jet exit were completely isolated from other synoptic systems [this is the case of Intensive Observation Period 17 (IOP17) of FASTEX and the Christmas storms of December 1999 studied in the paper].

Recent results from Ayrault (1998) and Ayrault and Joly (2000) emphasized the fact that although the strongest growth is not systematically located in regions of largest baroclinicity, the main factor responsible for cyclone growth is baroclinic interaction. Furthermore, some authors (e.g., Lee and Mak 1996) showed that the baroclinic generation rate tends to be localized downstream of the baroclinicity maximum. It seems that not much attention has been paid to these results on the location of the baroclinic generation rate, in part because of the emphasis made on downstream development. However, this peak of the baroclinic generation rate downstream of the baroclinicity maximum is confirmed in our case studies and the attempt of the paper is to describe mechanisms showing how the large-scale deformation field modulates baroclinic interaction and especially forces it to occur in some specific regions.

Our study is focused on reanalysis data of two different periods over the Atlantic area, one related to mid February 1997, which is a part of the FASTEX field phase, and another to the end of December 1999. These two periods are similar in the sense that they both correspond to a well established zonal regime (i.e., presence of a large-scale zonal jet) and they both lead to an explosive growth of extratropical cyclones at the jet exit; mid February 1997 was marked by a strong cyclone corresponding to IOP17 of FASTEX, which reached its amplitude maximum around Ireland and the end of December 1999 is a well-known period during which two extreme wind storms called Lothar and Martin devastated western Europe causing huge amounts of damage and having many human victims.

The study is presented as follows. Section 2 recalls some theoretical results developed in RHK03 and RHK04. Section 3 describes the methodology to adapt this quasigeostrophic theory to real case studies and the reanalysis data. It introduces a new diagnostic parameter called effective deformation. Section 4 is dedicated to prove the relevance of effective deformation. It also defines barotropic critical regions. Section 5 deals with the processes involved when such a region is collocated with the jet-exit region. Section 6 sums up the findings of this first part. The second part is dedicated to baroclinic development in jet-exit areas away from a barotropic critical region.

2. Theory of deformation field action in quasigeostrophic flows

All the following analytical results are detailed in RHK03 and RHK04 and are here briefly recalled. The following perturbation equations are obtained by decomposing the total flow into a reference flow (which satisfies momentum equations and whose quantities are denoted with overbars) and a perturbation (whose quantities are denoted with primes) and by linearizing the momentum equations. The kinetic energy equation within the quasigeostrophic framework can be written as

$$\frac{\overline{D}_g}{Dt} K'_{eg} = \mathbf{E}'_g \cdot \overline{\mathbf{D}}_g - \mathbf{u}'_g \cdot (-f_o \mathbf{k} \times \mathbf{u}'_a), \tag{1}$$

where $\mathbf{u}_g$ and $\mathbf{u}_a$ are the geostrophic and ageostrophic horizontal winds, respectively, $K'_{eg} \equiv \mathbf{u}'^2_g/2$ is the perturbation geostrophic kinetic energy, $\overline{D}_g/Dt = \partial/\partial t + \overline{\mathbf{u}}_g \cdot \boldsymbol{\nabla}$ is the geostrophic Lagrangian derivative, f_o is the Coriolis parameter, and $\mathbf{k}$ is the vertical unit vector. Here, $\mathbf{E}'_g$ and $\overline{\mathbf{D}}_g$ are defined as

$$\mathbf{E}'_g \equiv \left[\frac{1}{2}(v'^2_g - u'^2_g), \; -u'_g v'_g\right], \tag{2}$$

$$\overline{\mathbf{D}}_g \equiv \left(\frac{\partial \overline{u}_g}{\partial x} - \frac{\partial \overline{v}_g}{\partial y}, \frac{\partial \overline{v}_g}{\partial x} + \frac{\partial \overline{u}_g}{\partial y}\right), \tag{3}$$

where u_g and v_g are the two components of the geostrophic velocity, $\mathbf{E}'_g$ depends on the perturbation anisotropy, and $\overline{\mathbf{D}}_g$ is the deformation vector whose components are the stretching and shearing terms of the reference flow. The scalar product between $\mathbf{E}'_g$ and $\overline{\mathbf{D}}_g$ is the barotropic generation rate and enables the perturbation to barotropically extract energy from the reference flow (see Mak and Cai 1989). This mathematical formulation yields a simple interpretation; if the angle between $\mathbf{E}'_g$ and $\overline{\mathbf{D}}_g$ is acute, the perturbation extracts energy from the reference flow ($\mathbf{E}'_g \cdot \overline{\mathbf{D}}_g > 0$), whereas if the angle is obtuse, the perturbation loses energy to the reference flow ($\mathbf{E}'_g \cdot \overline{\mathbf{D}}_g < 0$). By noting that the modulus of the $\mathbf{E}'_g$ vector is the perturbation kinetic energy ($|\mathbf{E}'_g| = K'_{eg}$), and by defining $\overline{\sigma} \equiv |\overline{\mathbf{D}}_g|$ as the modulus of the $\overline{\mathbf{D}}_g$ vector, and ξ' as the angle such that $(\widehat{\overline{\mathbf{D}}_g, \mathbf{E}'_g}) \equiv \pi/2 + \xi'$ (where the $\widehat{\ }$ symbol represents the angle between the two vectors), the barotropic generation rate can be written as

$$\mathbf{E}'_g \cdot \overline{\mathbf{D}}_g = -K'_{eg} \overline{\sigma} \sin\xi'. \tag{4}$$

The sign of $\mathbf{E}'_g \cdot \overline{\mathbf{D}}_g$ depends directly on the angle ξ', whose time evolution equation can be derived from the linearized momentum equations under a Wentzel–Kramers–Brillouin (WKB) assumption [see Eq. (27) of RHK03]. The fixed points of the orientation equation;

that is, the angles satisfying the property $\overline{D}_g\xi'/Dt = 0$, are analyzed in RHK03. They are associated with an angle ξ' that does not evolve rapidly along a Lagrangian path; that is, correspond to a perturbation structure that is "in equilibrium" with the reference flow. There are two fixed points that are determined by

$$\xi' = \xi'^r_{\pm} \equiv \pm\arccos(-r), \tag{5}$$

where the parameter r has been introduced by Lapeyre et al. (1999) for studying potential vorticity gradient dynamics and depends solely on the reference flow properties

$$r \equiv \frac{\overline{\zeta} + 2\overline{D}_g\overline{\phi}/Dt}{\overline{\sigma}}. \tag{6}$$

Here, $\overline{\zeta}$ is the basic flow relative vorticity, and $-2\overline{D}_g\overline{\phi}/Dt$ is the rotation rate of the $\overline{\mathbf{D}}_g$ vector along a Lagrangian path since $(\widehat{\mathbf{O}_x, \overline{\mathbf{D}}_\mathbf{g}}) \equiv \pi/2 - 2\overline{\phi}$ is defined as the angle between the x axis and $\overline{\mathbf{D}}_g$ (see Fig. 1 of RHK03 for a representation of the angles); ξ'^r_-, which is an unstable fixed point, implies kinetic energy extraction from the reference flow to the perturbation and is hereafter called productive fixed point. By contrast, ξ'^r_+ is stable, leads to loss of perturbation kinetic energy, and is called destructive fixed point. If ξ' is equal to one of the fixed points, following Eq. (4), the exponential barotropic kinetic energy generation rate is equal to

$$\frac{\mathbf{E}'_g \cdot \overline{\mathbf{D}}_g}{K'_{eg}}(\xi' = \xi'^r_{\pm}) = \mp\sqrt{\overline{\sigma}^2 - \left(\overline{\zeta} + 2\frac{\overline{D}\,\overline{\phi}}{Dt}\right)^2} \tag{7}$$

and depends only on the reference flow properties.

The contraction (dilatation) axis corresponds to the direction of $\mathbf{u}'_g$ when $\mathbf{E}'_g$ is colinear to $\overline{\mathbf{D}}_g(-\overline{\mathbf{D}}_g)$, that is, when $\xi' = -\pi/2$ ($\xi' = \pi/2$). As the direction of $\mathbf{u}'_g$ with respect to the x axis forms an angle of $0.5(\xi' - 2\overline{\phi})$, the angle of the contraction (dilatation) axis with respect to the x axis is therefore equal to $0.5(-\pi/2 - 2\overline{\phi})$ $[0.5(\pi/2 - 2\overline{\phi})]$. The fixed points ξ'^r_- and ξ'^r_+ define two new axes whose angle with respect to the x axis are $0.5[-\arccos(-r) - 2\overline{\phi}]$ and $0.5[\arccos(-r) - 2\overline{\phi}]$, respectively, and differ from the dilatation and contraction axes in the general case where $r \neq 0$ [see Eq. (5)]. In the notions of dilatation/contraction axes, only the shearing and stretching terms contribute, whereas the deformation field has a rotational component that can modify the orientation of the perturbation anisotropy. This rotational component, expressed as the sum $\overline{\zeta} + 2\overline{D}_g\overline{\phi}/Dt$ and called effective rotation rate, indirectly modifies the barotropic generation term [see Eq. (7)]. In the case where the rotation term $\overline{\zeta} + 2\overline{D}_g\overline{\phi}/Dt$ is larger than the deformation magnitude $\overline{\sigma}$, no fixed points exist as the rotation action is so strong that the perturbation cannot be elongated along a given axis. In other words, in the latter regions, the shape of the perturbation is almost isotropic and barotropic processes are therefore quite weak.

3. Methodology

To apply the previous quasigeostrophic theory to reanalysis data, it is necessary to decompose the atmospheric flow into two parts, one corresponding to the reference flow and the other to the perturbation. We will consider the classical decomposition into a low-frequency part and a high-frequency part (see, e.g., Orlanski and Katzfey 1991; Ayrault 1998; Lackmann et al. 1999) that separates the synoptic signal from its environment. The temporal filter used is quite simple as the low-frequency field is defined as the time mean over 8 days of the total field centered on the current date and the high-frequency field is the subtraction of the total field from the low-frequency one. As one week is the typical time scale of a weather regime (Vautard 1990) and a synoptic signal has usually a period of 2–6 days, a time mean over 8 days filters the synoptic signal and leads to the flow related to the weather regime. Note that tests have shown little sensitivity to this choice of filter and parameters. With the help of the theory previously described, our study thus focuses on the influence of the low-frequency flow (denoted hereafter with subscript m) and especially the impact of its deformation field on the high-frequency cyclones (denoted hereafter with primes).

a. Application of the theory

Following the previously mentioned decomposition, bars are replaced by the subscript m and the barotropic generation rate in spherical coordinates can be expressed as $\mathbf{E} \cdot \mathbf{D}_m$, where $\mathbf{E} \equiv [\frac{1}{2}(v'^2 - u'^2), -u'v']$ and $\mathbf{D}_m \equiv (\partial u_m/\partial x - \partial v_m/\partial y - v_m \tan\varphi/a, \partial v_m/\partial x + \partial u_m/\partial y + u_m \tan\varphi/a)$. Variables u and v are the two horizontal velocity components, φ is latitude, a is the radius of the earth, $\partial/\partial x \equiv (a\cos\varphi)^{-1}\,\partial/\partial\lambda$ and $\partial/\partial y \equiv a^{-1}\partial/\partial\varphi$ are the horizontal derivatives and λ is longitude. The new formula of Eqs. (5), (6), and (7) in spherical coordinates involve the modulus of the deformation vector $\sigma_m \equiv |\mathbf{D}_m|$ and the effective rotation rate $\zeta_m + 2D_m\phi_m/Dt$. Also, $\zeta_m \equiv \partial v_m/\partial x - \partial u_m/\partial y - u_m \tan\varphi/a$ is the rotation rate relative to the basis set $(\mathbf{i}, \mathbf{j})$ where $\mathbf{i}$ and $\mathbf{j}$ are the unit vectors directed eastward and northward and $2\phi_m$ is defined as $(\widehat{\mathbf{i}, \mathbf{D}_m}) \equiv \pi/2 - 2\phi_m$ [see Koh and Legras (2002) for the details leading to the decomposition of the effective rotation rate in spherical coordinates].

The rotation rate of the deformation vector $2D_m\phi_m/Dt$ is strong when the reference flow has a strong curvature as it is the case, for example, when the reference flow is composed of isolated eddies (Lapeyre et al. 1999). But if the flow is composed of a straight zonal jet varying with latitudes; that is, whose velocity components are defined as $(u_m, v_m) = [U(y), 0]$, then ζ_m equals to $-\partial_y U - U \tan \varphi/a$ and the rotation rate of the deformation vector $2D_m\phi_m/Dt$ is exactly zero. The reference flow is here composed of a weakly curved jet stream and the term $2D_m\phi_m/Dt$ can be therefore neglected. The fixed points of Eq. (5) can be thus simplified to $\xi^r_\pm \simeq \pm\arccos(-\zeta_m/\sigma_m)$ and a new diagnostic parameter, called hereafter effective deformation and denoted Δ_m, is introduced following expression (7):

$$\Delta_m \equiv \sigma_m^2 - \zeta_m^2. \tag{8}$$

When Δ_m is positive, preferred shapes of the perturbation with respect to the principal axes of deformation do exist according to the previous section. This in turn activates barotropic energy processes such that the rate of conversion is $\pm K'_e\sqrt{\Delta_m}$, where $K'_e \equiv \frac{1}{2}(u'^2 + v'^2)$ is the eddy kinetic energy. The usual diagnostics to estimate the deformation action comprise the dilatation/contraction axes [defined as the angle $0.5(\pm\pi/2 - 2\phi_m)$ with respect to the x axis] and the large values of the deformation magnitude σ_m (Black and Dole 2000). By contrast, the new parameters suggested by the RHK theory are composed of the fixed points directions (defined as the angle $0.5[\pm\arccos(-\zeta_m/\sigma_m) - 2\phi_m]$ with respect to the x axis) and the large values of the effective deformation Δ_m. The additional ingredient in Δ_m is the vorticity ζ_m and the inclusion of all the horizontal inhomogeneities of the low-frequency flow as the stretching, shearing and vorticity terms appear in our definitions; that is, all the horizontal derivatives of the horizontal wind. A summary of these results are presented in Fig. 1. The dynamical role played by regions of positive Δ_m in the cyclone life cycles is analyzed in the next section.

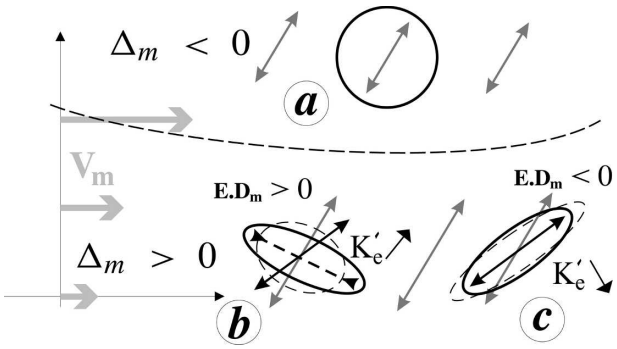

FIG. 1. Schematic illustrating the relationship between the effective deformation $\Delta_m = \sigma_m^2 - \zeta_m^2$, where m indicates a large-scale component of the flow obtained as a time mean, and synoptic-scale perturbations. The latter are represented as single contour vorticity maxima (heavy solid black line at a given time and solid dash line at a later time). The gray double arrows represent the large-scale dilatation axes related to the large-scale wind $\mathbf{V}_m$ and corresponding deformation σ_m. (a) Here, $\Delta_m < 0$, vorticity effects dominate, there is no preferred shape for perturbations and therefore no preferred barotropic energy exchanges. Where $\Delta_m > 0$, deformation effects dominate with in particular two equilibrium orientations for perturbations. The double black solid (dash) arrows represent the stable (unstable) equilibrium orientation leading to perturbation decay (growth). (b) This configuration is efficient for the perturbation to grow barotropically ($\mathbf{E} \cdot \mathbf{D}_m > 0$); the perturbation is being compacted but the growth is transient or unsettled. (c) This configuration is efficient for the perturbation to decay barotropically ($\mathbf{E} \cdot \mathbf{D}_m < 0$); the perturbation is being elongated along the stable axis and its decay is settled.

b. Dataset

The dataset used for the period of FASTEX is extracted from the reanalysis done with the Météo-France operational 4DVAR Action des Recherches Petite Echelle et Grande Echelle (ARPEGE) system (Desroziers et al. 2003). The present study focuses on the period going from 12 to 28 February 1997 during which a zonal regime was well established. The data for the period of December 1999 going from 23 to 28 December is obtained from the same codes as those of the 4DVAR reanalysis of FASTEX.

4. Barotropic critical regions

Figure 2 is a comparison between the horizontal inhomogeneities of the two low-frequency jets of mid-February 1997 (left column) and the end of December 1999 (right column) and emphasizes the new information brought by the effective deformation on jet asymmetries.

a. Spatial distribution of the effective deformation Δ_m

The low-frequency effective deformation Δ_m (Fig. 2c) is now compared to the square of the deformation magnitude, σ_m^2 (Fig. 2a) for the mid-February case. The large difference between the two patterns proves that the low-frequency vorticity ζ_m reaches values as large as those of the deformation magnitude σ_m. The quantity Δ_m has three distinct regions with large positive values along the jet (see Fig. 2c): one located at the jet en-

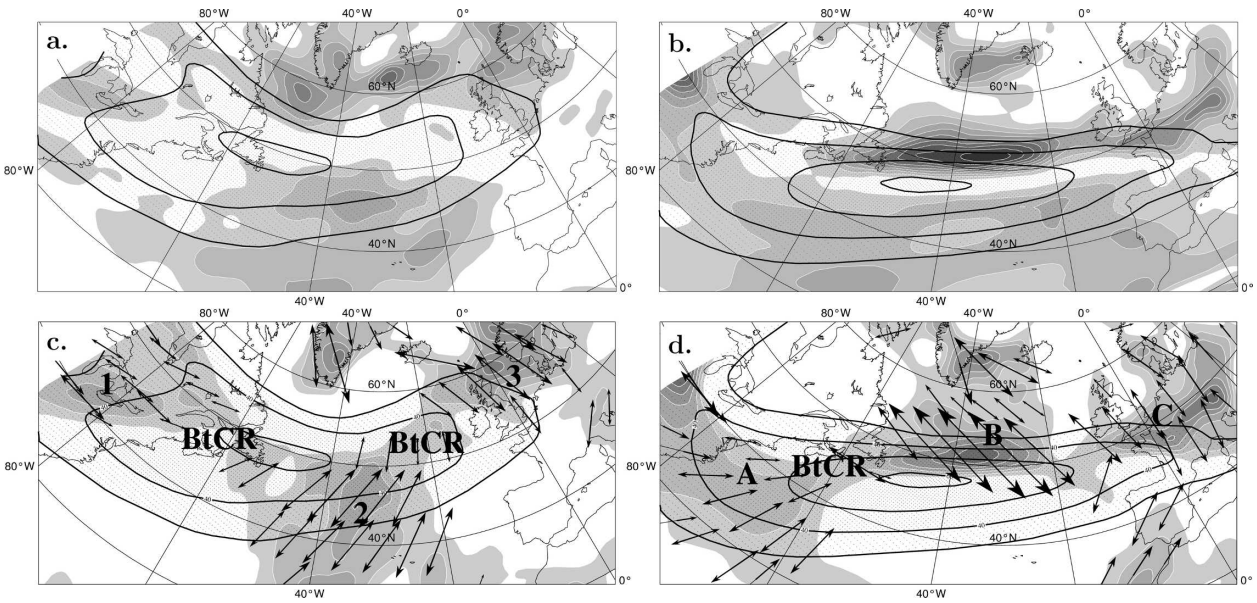

FIG. 2. Horizontal inhomogeneities of the low-frequency jet (350 hPa) at (a), (c) 0000 UTC 19 Feb 1997 and (b), (d) 0000 UTC 26 Dec 1999; (a), (b) wind speed $|\mathbf{u}_m|$ larger than 30 m s^{-1} (dotted shadings and solid contours, interval 10 m s^{-1}) and the square of the deformation magnitude σ_m^2 larger than 5×10^{-10} s^{-2} (shaded contours, interval 5×10^{-10} s^{-2}); (c), (d) $|\mathbf{u}_m|$ and the positive values of the low-frequency effective deformation Δ_m (shaded contours, interval 5×10^{-10} s^{-2}) superposed to the dilatation axes in regions where $\Delta_m > 0$ (arrows).

trance (region 1), another halfway of the jet zonal extent on its anticyclonic (warm) side (region 2), and the last one at the jet exit on its cyclonic (cold) side (region 3).[1] Between longitudes 60° and 20°W, the deformation magnitude has strong values north of the jet (see Fig. 2a), whereas the Δ_m field exhibits positive values south of the jet (region 2 in Fig. 2c). It means that the amplitude of ζ_m matches or exceeds the deformation magnitude on the cyclonic side. This result is logical as the jet has globally a slight cyclonic curvature leading to large values of vorticity on its northern side. It shows also that regions of positive values of Δ_m do not necessarily correspond to regions where the horizontal gradients are the strongest. Finally, region 3 located downstream of the jet exit is, by contrast with region 2, characterized by large values of the deformation and is located on the cyclonic side of the jet.

The low-frequency jet at 0000 UTC 26 December 1999 (right column of Fig. 2) is much stronger than that of mid-February 1997 and has a stronger deformation magnitude too. But despite this difference in amplitudes, maxima of σ_m are located on the northern side of the jet in both cases and so is the overall distribution of vorticity. Nonetheless, the two Δ_m fields differ both in amplitude and location. Indeed, in the region where the jet of December 1999 reaches its maximum speed; that is, between 50° and 20°W, Δ_m is positive on the northern side (region B in Fig. 2d) whereas it is the same on the southern side for February 1997 (region 2 in Fig. 2c). In other words, although the spatial distributions of σ_m and ζ_m are similar along quasi-zonal jet flows and differ only in magnitude, the effective deformation highlights a level of variability so far unnoticed, yet of great consequence on the synoptic-scale variability as shown below.

In Figs. 2c and 2d, the dilatation axes are plotted in regions where Δ_m is positive, which allows the introduction of the notion of barotropic critical regions (denoted BtCR). A BtCR is defined as a bottleneck area between two regions of positive Δ_m where the dilatation axes are almost perpendicular upstream and downstream of it. The area about the limit points between regions 1 and 2 and between regions 2 and 3 (see Fig. 2c) are therefore defined as BtCR regions as well as that between regions A and B (see Fig. 2d). But the point between regions B and C is not a BtCR region as B and C are both located on the northern side of the jet and the dilatation axes have almost the same northwest–southeast (NW–SE) direction inside each region. To emphasize the dynamical role of the BtCR regions is the aim of the present paper.

[1] The word cyclonic (anticyclonic) comes from the fact that on the north (south) side of the jet, relative vorticity is positive (negative; see Thorncroft et al. 1993).

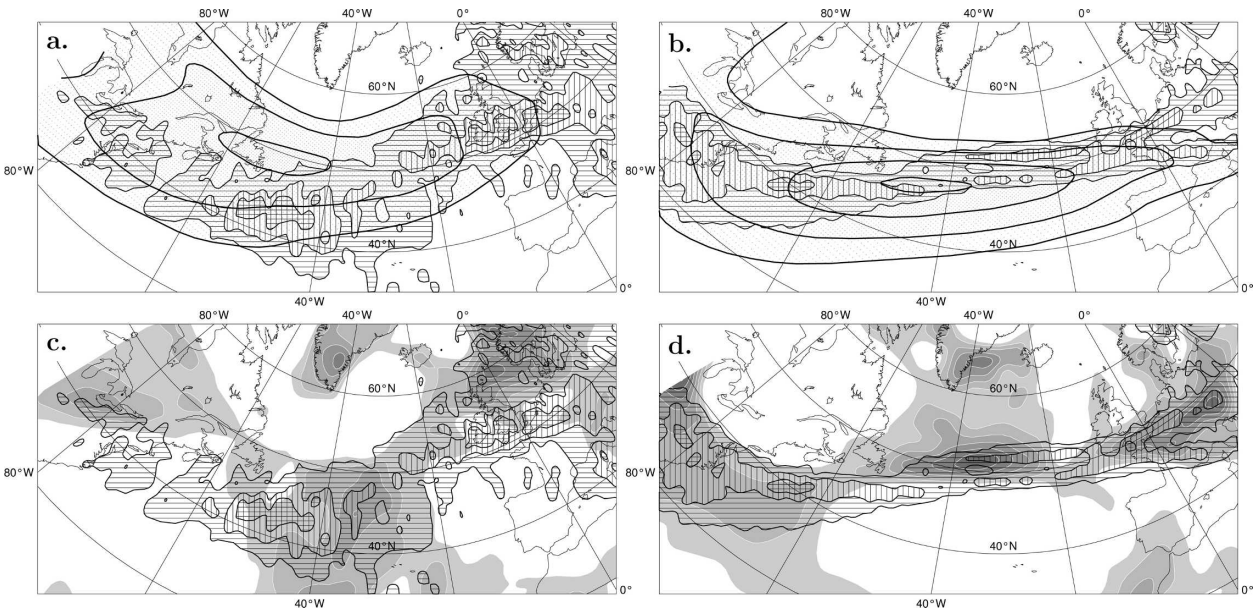

FIG. 3. At 350 hPa, high-frequency relative vorticity density (hatched shadings, definition given in the text) during (a), (c) 12–28 Feb 1997 and (b), (d) 23–28 Dec 1999; (a), (b) wind speed $|\mathbf{u}_m|$ larger than 30 m s^{-1} (dotted shadings and black contours, interval 10 m s^{-1}) for the two periods; (c), (d) positive values of Δ_m (shaded, white contours, interval 5×10^{-10} s^{-2}) for the two periods.

b. Location of perturbations and the effect of crossing a BtCR

Figure 3 compares the spatial structure of the low-frequency jet with the high-frequency relative vorticity density at 350 hPa for the two different periods. The density is defined in the appendix and is obtained by counting at each grid point the number of times the high-frequency relative vorticity is above a given threshold (here 1.2×10^{-4} s^{-1}) during the period considered. This threshold of 1.2×10^{-4} s^{-1} is reasonable for the upper-tropospheric high-frequency relative vorticity to detect the most significant disturbances and different threshold conditions have been tested above this value leading to the same results. For the two seemingly similar zonal flows of February 1997 and December 1999, as far as the overall structure is concerned, the upper-level synoptic activity displays two different spatial locations. In short, synoptic perturbations move from the warm to the cold side of the low-frequency jet on its eastern and exit area for the first flow. The same transition occurs along the December 1999 jet but on the entrance and western half. While this behavior appears difficult to relate to the distributions of large-scale deformation and vorticity (differing only in magnitude), the comparison of the density distribution with effective deformation reveals a close match of the two patterns. This suggests the relevance of positive areas of effective deformation as the preferred path of perturbations. As a result, barotropic critical regions between regions 2 and 3 and between A and B correspond to the specific regions where the high-frequency disturbances tend preferentially to cross the jet during the two periods considered. A more quantitative comparison between the high-frequency disturbances location and the effective deformation is done as follows; by considering the grid points where the high-frequency relative vorticity exceeds a given threshold, the percentage of those belonging to a region where Δ_m is positive is computed. For a threshold of 10^{-4} s^{-1}, the percentage for the February 1997 regime is 60% and is 68% for the other regime. These percentages slightly increase by increasing the threshold. The quantity Δ_m is therefore relevant to localize the spatial distribution of the most important high-frequency disturbances relatively to the low-frequency jet core. The deformation magnitude does not offer such a predictor.

Moving from a measure of overall perturbations activity to one such structure, consider now the dynamical importance of BtCR regions in its evolution. Figure 4 is a sketch presenting three stages in the evolution of a perturbation as a consequence of the theory and facts presented up to now. Step 1, the perturbation is on the anticyclonic side of the jet and upstream of the BtCR region. It is stretched along the stable preferred orientation of section 2 that leads to barotropic decay and which is oriented SW–NE in this region. Since perturbations remain in areas of positive Δ_m, as just shown, this one crosses the jet about the BtCR region (step 2),

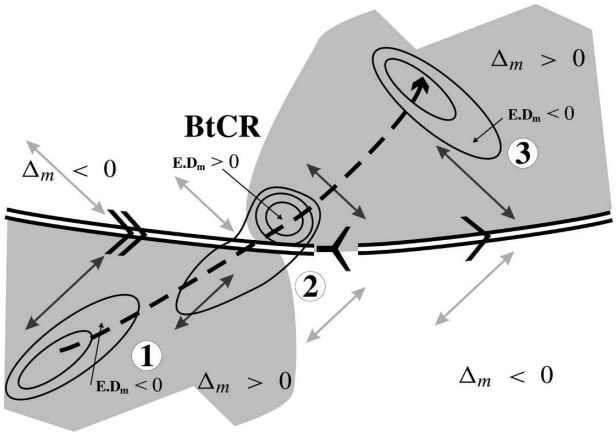

FIG. 4. Schematic depicting the large-scale flow configuration making a BtCR and the evolution of a perturbation moving through this region. The large-scale features are a diffluent jet flow, symbolized by the heavy solid double line and the rotated Y-shaped symbol, following the proposal for representing upper-air features of Santurette and Joly (2002). The symbol marks the main jet exit. The gray shaded areas indicate zones where $\Delta_m > 0$, namely, where the modulus of the large-scale deformation σ_m is larger than vorticity ζ_m, the double arrows are the associated dilatation axes, darker in zones where $\Delta_m > 0$. The main characteristic is that the $\Delta_m > 0$ area downstream of the jet exit is on the cyclonic side while it is on the anticyclonic side upstream. The bold solid contours stand for the vorticity or geopotential of a perturbation, and its evolution is represented in a three-step sequence making a trajectory indicated by the bold dashed line. The sequence presents a transient barotropic phase about the BtCR area, which is detailed in the text.

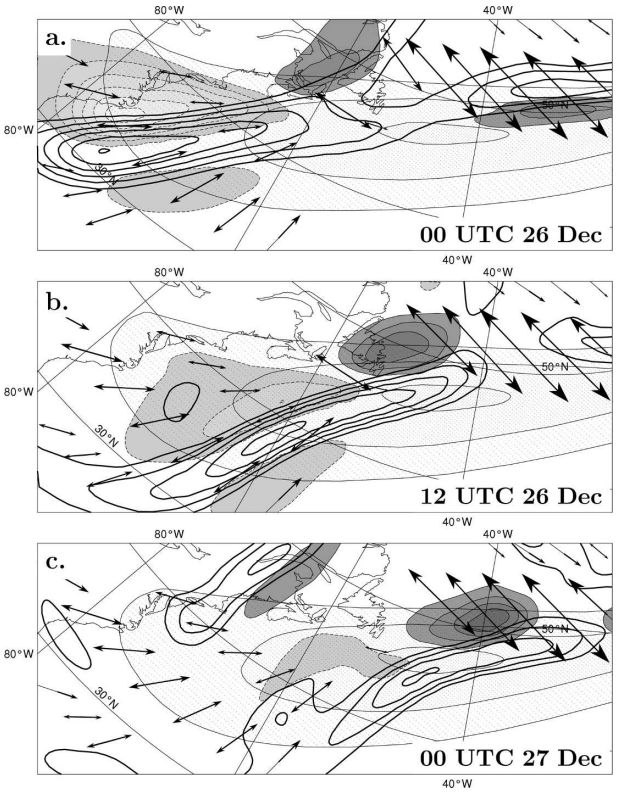

FIG. 5. At the level 350 hPa, barotropic generation rate (interval 0.01 m^2 s^{-3}, light shadings with dashed contours for negative values and dark shadings with solid contours for positive values), low-frequency wind speed $|\mathbf{u}_m|$ larger than 40 m s^{-1} (dotted shadings), the high-frequency relative vorticity larger than 5×10^{-5} s^{-1} (thick solid contours, interval 5×10^{-5} s^{-1}), and the dilatation axes in regions where $\Delta_m > 0$ (black arrows) at (a) 0000 UTC 26 Dec, (b) 1200 UTC 26 Dec, and (c) 0000 UTC 27 Dec.

its environment is drastically modified with a sudden change of the preferred axes. The result is that its elongated structure is parallel to the productive axes downstream of the BtCR region but still parallel to the destructive ones upstream of it leading to an intensification of the perturbation downstream and to a disappearance of it upstream. The perturbation intensification downstream of a BtCR region is only transient as the productive fixed point is an unstable fixed point. The perturbation then tends to be stretched again along the destructive orientation but as it is now located on the cyclonic side of the jet its orientation is NW–SE (step 3). The conditions about a BtCR suggest that such a behavior is quite general. A BtCR area is thus a latent place for transient barotropic increase.

Figure 5 gives a first illustration of these processes. It focuses on an upper-level disturbance evolving around the BtCR region separating regions A and B and is precisely the upper-level precursor leading to the storm Martin that hit France on 27 December 1999. At 0000 UTC 26 December (Fig. 5a), the disturbance is entirely on the anticyclonic side of the jet (region A) and is strongly stretched along the dilatation axes. In this case, the dilatation axis and the destructive stable axis of section 2 are almost parallel. This situation corresponds to step 1 of Fig. 4; a large barotropic sink occurs and the amplitude of the southern part of the upper-level disturbance decreases. But when the perturbation enters region B, the high-frequency isolines are perpendicular to the dilatation axes as in step 2 of Fig. 4 leading to barotropic increase in this new area (see Figs. 5a,b). At 0000 UTC 27 December (Fig. 5c), much of the high-frequency disturbance is already on the cyclonic side and still increases barotropically. This barotropic mechanism explains why the high-frequency structure disappears on the anticyclonic side and appears on the other side. The following section depicts the same behavior at low levels and indicates how this can lead to a more dramatic impact.

5. Barotropic triggering of a baroclinic development phase

This section is dedicated to introducing a detailed mechanism of how moving into a BtCR can trigger a phase of rapid development. It is illustrated with the last growth stage of the FASTEX IOP17 cyclone at the jet exit.

a. Revised energy conversions' definitions

Prior to this, it is useful to revise and to complete the energy-related definitions required in the real-case framework. The high-frequency eddy kinetic energy equation deduced from the primitive momentum equations in isobaric coordinates can be expressed as

$$\frac{D_m}{Dt} K'_e = -\mathbf{u}' \cdot \boldsymbol{\nabla}_p \Phi' - \mathbf{u}' \cdot (\mathbf{u}'_3 \cdot \boldsymbol{\nabla}_3 \mathbf{u}_m) + R_1, \quad (9)$$

where Φ is the geopotential, $\mathbf{u}_3$ is the three-dimensional velocity vector, $\mathbf{u}$ is the horizontal velocity vector, $D_m/Dt = \partial/\partial t + \boldsymbol{\nabla}_3 \mathbf{u}_{3m}$. Here, $\boldsymbol{\nabla}_3$ is the three-dimensional Lagrangian derivative, $\boldsymbol{\nabla}_p$ is the horizontal component of the three-dimensional gradient operator in isobaric coordinates ($\boldsymbol{\nabla}_3 = \boldsymbol{\nabla}_p + \mathbf{k}\partial/\partial p$). The first two terms of the right-hand side are the pressure work and the Reynolds stress term, respectively. All the other terms are included in the residual term, denoted R_1, which is composed of dissipation, forcing, and nonlinear eddy terms (see, for more details, Orlanski and Katzfey 1991).

The Reynolds stress term can be expressed as follows (see Lackmann et al. 1999):

$$-\mathbf{u}' \cdot (\mathbf{u}'_3 \cdot \boldsymbol{\nabla}_3 \mathbf{u}_m) = \mathbf{E} \cdot \mathbf{D}_m - K'_e(\boldsymbol{\nabla}_p \cdot \mathbf{u}_m) - \omega'\left(\mathbf{u}' \cdot \frac{\partial \mathbf{u}_m}{\partial p}\right). \quad (10)$$

The barotropic generation rate $\mathbf{E} \cdot \mathbf{D}_m$ has been already shown to be important for the appearance of new disturbances in the upper troposphere (Lackmann et al. 1999; Kucharski and Thorpe 2000), as confirmed in Fig. 5 above. It is the only term of the Reynolds stress that intervenes in quasigeostrophic dynamics and is usually the predominant term of the Reynolds stress in real case studies.

The pressure work term can be written as the sum of three terms

$$-\mathbf{u}' \cdot \boldsymbol{\nabla}_p \Phi' = -\boldsymbol{\nabla}_p \cdot (\mathbf{u}'\Phi') - \frac{\partial(\omega'\Phi')}{\partial p} - \mathcal{R}\theta'\omega', \quad (11)$$

where $\mathcal{R} \equiv R/p\,(p/p_0)^{(C_v/C_p)}$, θ is the potential temperature, ω is the vertical velocity in pressure coordinates, R is the gas constant, p_0 is a reference pressure, C_v and C_p are the specific heats of the air, at constant volume and pressure. The first two terms in the right-hand side are, respectively, the ageostrophic geopotential horizontal and vertical fluxes that redistribute horizontally and vertically eddy kinetic energy. Ageostrophic geopotential horizontal fluxes may play a crucial role in the growth of some cyclones as shown by Orlanski and Katzfey (1991) and Orlanski and Sheldon (1995). The third term, $-R\theta'\omega'$, is the baroclinic conversion rate from eddy potential energy to eddy kinetic energy and is generally strong when an upper disturbance interacts baroclinically with a surface cyclone.

Another term to measure baroclinic interaction is the baroclinic potential energy generation rate that enables eddies to extract available potential energy from the time-mean flow. It intervenes in the eddy potential and total energy equations and can be expressed as

$$\frac{-1}{S}\left(\theta' v' \frac{\partial \theta_m}{\partial y} + \theta' u' \frac{\partial \theta_m}{\partial x}\right) = T'_e |\mathbf{B}_c| \mathrm{conf} \equiv T'_e |\mathbf{B}_c| \frac{\dfrac{1}{\sqrt{S}}\theta'(v', -u') \cdot \mathbf{e}_c}{\dfrac{1}{2}(u'^2 + v'^2) + \dfrac{1}{2S}\theta'^2}, \quad (12)$$

where $S \equiv -\mathcal{R}^{-1}(\partial\theta_0/\partial p)$, θ_0 is the potential temperature average at the given level p, $\mathbf{B}_c \equiv (1/\sqrt{S})[-(\partial\theta_m/\partial y), (\partial\theta_m/\partial x)]$ is the baroclinicity vector, $\mathbf{e}_c \equiv \mathbf{B}_c/|\mathbf{B}_c|$ its unit vector and $T'_e \equiv \frac{1}{2}(u'^2 + v'^2) + (1/2S)\theta'^2$ is the eddy total energy. This decomposition introduces the configuration term, denoted conf in Eq. (12), which is a useful term to measure the efficiency of the baroclinic interaction. Indeed, baroclinic interaction can be weak in a strong baroclinicity environment, if the baroclinic configuration, say between an upper disturbance and a surface cyclone, is not optimal and leads to weak values of conf. The instantaneous optimal baroclinic configuration is obtained when conf equals one.

b. Last growth stage of FASTEX IOP17 at the jet exit

The surface low development associated with IOP17 is essentially decomposed into an initiation stage from 1200 UTC 16 February to 1200 UTC 17 February, a first growth stage ending at 1200 UTC 18 February, a period of decrease until 0000 UTC 19 February, a second growth stage ending at about 0000 UTC 20 February and finally decreasing. Despite its strong deepening during its second growth stage, most of the papers on the IOP17 cyclone have studied its initiation stage or its first growth stage [see Mallet et al. (1999a) and Arbogast (2004) for the initial formation of the low-level

precursor; see Kucharski and Thorpe (2000) for the initial formation of the upper-level disturbance; and Cammas et al. (1999) and Mallet et al. (1999b) for the first baroclinic stage of growth and the important role played by the diabatic heating]. Our study will focus on the dynamical processes leading to the last growth stage in the jet-exit region that have not been yet studied. In what follows, the notations Day1, Day2, and Day3 refer to 18, 19, and 20 February, respectively.

1) ROLE OF THE BAROTROPIC CRITICAL REGION

Figure 6 is an overview of the large-scale conditions in which IOP17 is embedded during its second growth stage. It occurs in a region located downstream of the low-frequency baroclinicity maximum and during this phase its trajectory goes from region 2 to region 3 and crosses the BtCR region. When IOP17 crosses the jet about the BtCR, the low-frequency barotropic environment changes drastically as the dilatation axes change suddenly their orientation. Figure 6 suggests therefore that the barotropic environment may play an important role in the last development of IOP17.

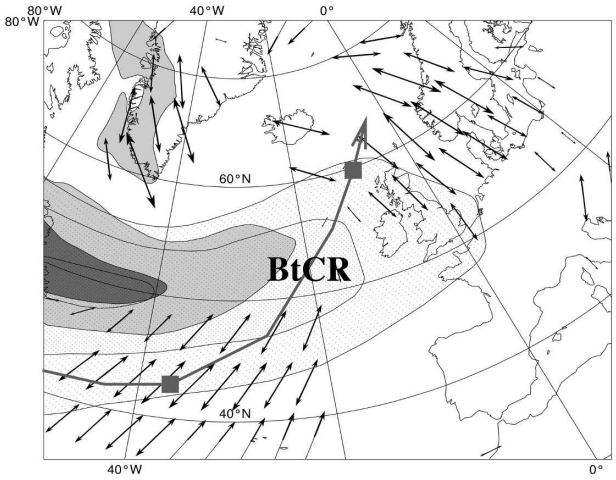

FIG. 6. Trajectory of IOP17 of FASTEX in the jet-exit region (large gray arrow). The gray squares correspond to its positions at 1800 UTC Day1 and 0000 UTC Day3. Vertically averaged (900–200 hPa) low-frequency baroclinicity $|\mathbf{B}_c|$ larger than 3×10^{-5} s^{-1} (shaded contours, interval 10^{-5} s^{-1}), wind speed $|\mathbf{u}_m|$ at 350 hPa larger than 30 m s^{-1} (dotted shadings and light black contours, interval 10 m s^{-1}), and vertically averaged dilatation axes (black double arrows) in regions where Δ_m is positive at 0000 UTC Day2.

Figure 7 is a schematic describing how a BtCR region can trigger a baroclinic growth stage of a cyclone. The surface cyclone now considered still evolves according to the different steps of Fig. 4 but it also interacts with an upper-level disturbance during its life cycle. The new aspect is that the rapid deepening of the surface low at step 2 on its downstream edge implies a new vertical tilt of the compound perturbation system. This change of the vertical structure then allows for a reinforced or even new phase of baroclinic growth, which is able to develop the system much more efficiently than the barotropic phase prior to it (step 3). Once well within the downstream zone of $\Delta_m > 0$ at both level, the cyclone resumes a shape that implies barotropic loss of energy, with a weak or zero baroclinic gain (step 4). A BtCR region has a direct effect by stopping transiently the barotropic sink, but can also have an indirect effect by changing the baroclinic configuration between an upper disturbance and a surface cyclone that makes possible a new baroclinic development phase.

Figure 8 provides an actual realization of this mechanism by describing the end of the IOP17 life cycle as derived from the time filtered fields. At 1800 UTC Day1 (Fig. 8a), the system of interest (in the lower-left side of the figure) is well developed with an upper-level disturbance weakly interacting baroclinically with the surface cyclone, which can be seen from the slight downstream location of the low-level geopotential trough relative to its upper-level counterpart. Note also that there is another high-frequency system in the upper-right-hand-side of the figure. These two systems are on two different sides of the jet, and they take on two shapes with characteristics horizontal tilts that can be interpreted by the action of stretching along the dilatation axes on both sides of the jet. Six hours later (Fig. 8b), the amplitudes of the two low-level systems have decreased and their larger elongation along the dilatation axes suggests that the decrease is due to negative barotropic conversion. At 0000 UTC Day2 (Fig. 8b), a new local geopotential minimum appears at the northeastern tip of the low-level component of IOP17 similarly to step 2 of Fig. 7. This new minimum downstream of the whole synoptic system is strongly reinforced at 0600 UTC Day2 (Fig. 8c) whereas the original one disappears. This is followed by a rapid change of the surface cyclone anisotropy from 1800 UTC Day1 to 1200 UTC Day2 that coincides with the crossing of the jet around BtCR.

Because of the rapid appearance of the second minimum at 900 hPa downstream of the whole synoptic system, the relative distance between the geopotential minima at 350 and 900 hPa increases strongly between 1800 UTC Day1 and 1200 UTC Day2. It shows that the tilt with height of the geopotential isolines increases too and suggests a restarting of the baroclinic interaction between the upper disturbance and the surface cyclone. At 0000 UTC Day3 (Fig. 8f), the cyclone reaches its maximum amplitude and begins to stretch along a SE–NW axis, which is even more visible 6 and 12 h later

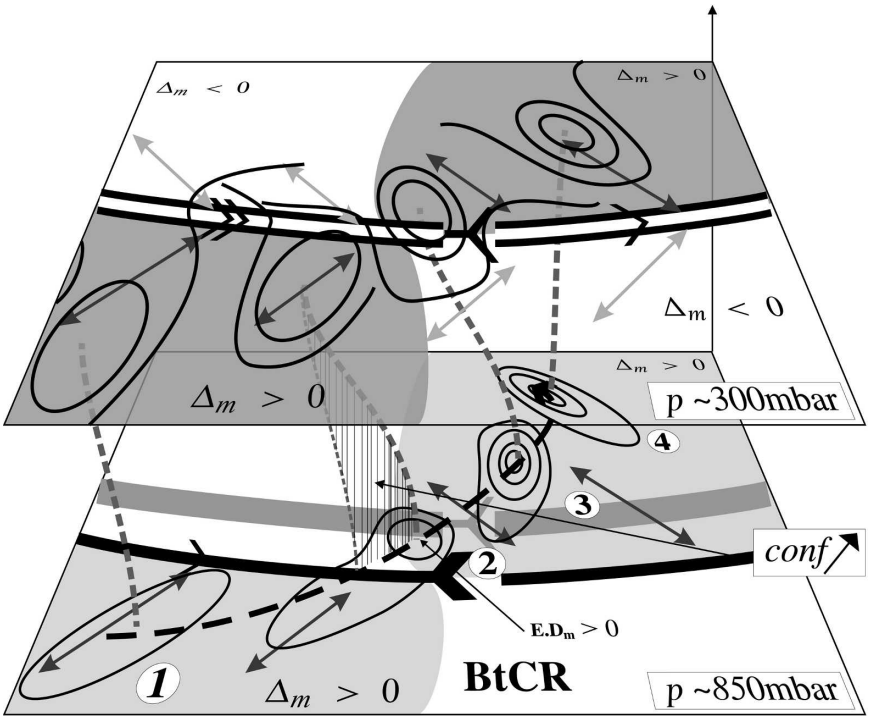

FIG. 7. Schematic summarizing how a BtCR, defined in Fig. 4, present throughout the troposphere, can trigger a phase of rapid baroclinic growth in the life cycle of a midlatitude cyclone. The upper-level jet and significant diffluent zone are indicated by the heavy double black line and rotated Y-shaped symbol, respectively, that projects as a gray heavy line on the lower level. At that same low level, there is also a large-scale flow shown by the single heavy black line with the same diffluent feature. The double arrows stand for the large-scale dilatation axis. At both levels, areas where $\Delta_m > 0$ appear as gray shaded. See text for a detailed description of the four-step sequence.

(not shown). This strong elongation along the dilatation axis suggests large negative barotropic generation rates and could explain the decrease of the synoptic system after 0000 UTC Day3. This dynamical description of the second stage of growth of IOP17 is similar to the different steps of our schematic picture of Fig. 7 and is now quantitatively checked.

Barotropic conversion rates at low levels between 1800 UTC Day1 and 0600 UTC Day2 are presented in more details in Fig. 9. Note that the sum of $\mathbf{E} \cdot \mathbf{D}_m$ and the divergence term $-K'_e(\nabla_p \cdot \mathbf{u}_m)$ is plotted because the two terms act in the same way but as shown below the essential signal comes from the classical term $\mathbf{E} \cdot \mathbf{D}_m$. The time evolution of the surface cyclone represented here by the high-frequency geopotential is similar to the schematic picture of Fig. 4. First, it confirms that the temporary decrease of the cyclone between 1800 UTC Day1 and 0000 UTC Day2 due to barotropic decrease is largely stopped when it crosses the low-level jet. Second, the downstream appearance of a local minimum of geopotential and its rapid reinforcement is well explained by barotropic generation of kinetic energy.

2) ENERGY BUDGET

An energy budget analysis is performed every 6 h over a control volume made up of a cylinder centered around IOP17. Although energy and conversions values depend on the control volume, their relative magnitudes and signs are rather insensitive to it, provided that the cylinder remains focused on the system of interest. More precisely, each quantity is first vertically averaged between two isobars and then averaged over a circle whose center is precisely the center of gravity around IOP17 of the vertically averaged energetic quantity considered, and whose radius corresponds to 13° in latitude.

Figure 10 is an energy budget analysis that details the evolution of the high-frequency kinetic energy K'_e associated with IOP17. Let us first interpret the evolution of the averaged kinetic energy over the entire troposphere by looking at Figs. 10a,b,c. The different stages of

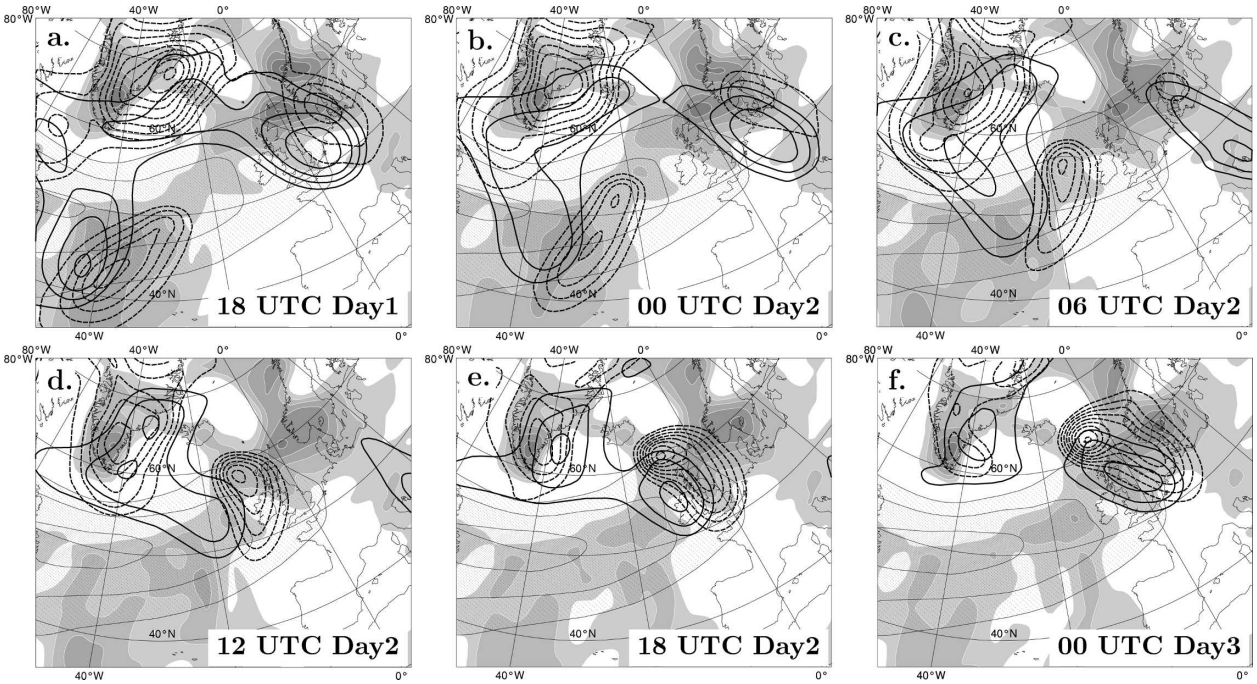

FIG. 8. Low-frequency wind speed $|\mathbf{u}_m|$ at 350 hPa larger than 30 m s^{-1} (dotted shadings and light contours, interval 10 m s^{-1}), positive values of Δ_m at 350 hPa (shaded, white contours, interval 5×10^{-10} s^{-2}), negative values of the high-frequency geopotential at 350 hPa (thick solid contours, interval 500 m^2 s^{-2}) and of the high-frequency geopotential at 900 hPa (thick dashed contours, interval 250 m^2 s^{-2}): (a) 1800 UTC Day1, (b) 0000 UTC Day2, (c) 0600 UTC Day2, (d) 1200 UTC Day2, (e) 1800 UTC Day2, and (f) 0000 UTC Day3.

IOP17 evolution described in the beginning of section 5b (two growth stages and two decrease stages) are clearly identified in Fig. 10a as the K'_e curve has two well-defined peaks. The pressure work in Fig. 10b has a significant positive sign during the whole evolution and decreases only slightly from 1200 UTC Day1 to the end. By contrast, the Reynolds stress term which is completely dominated by the barotropic generation rate $\mathbf{E} \cdot \mathbf{D}_m$ (see Fig. 11), is almost negative at each time except at 1800 UTC Day2 where it is slightly positive and has strongly increased during the previous 24 h, which corresponds to the crossing of the BtCR region by IOP17. The sum of the two terms has a well-defined positive peak at 1800 UTC Day2 that remarkably fits the 12-h kinetic energy increase starting 1200 UTC Day2. This positive peak is essentially due to the interruption of the barotropic decrease and to the relatively constant positive sign of the pressure work. The pres-

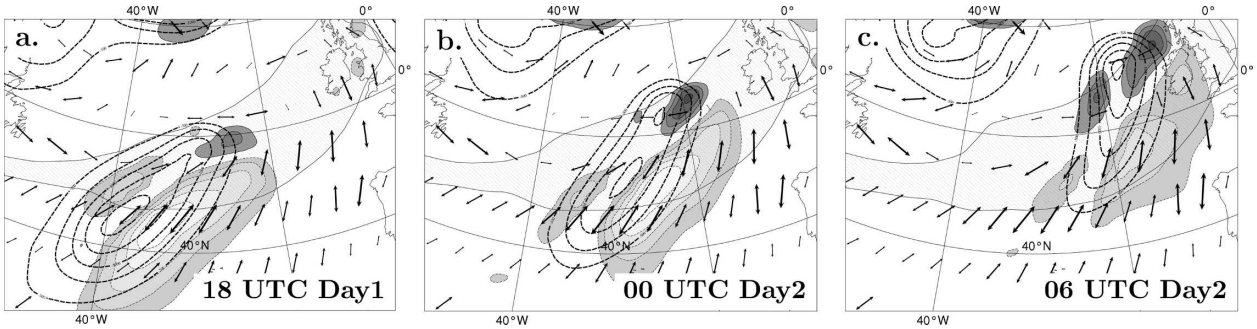

FIG. 9. At 900 hPa, barotropic generation rate $\mathbf{E} \cdot \mathbf{D}_m - K'_e(\nabla_p \cdot \mathbf{u}_m)$ (interval 1.5×10^{-3} m^2 s^{-3}, light shadings with dashed contours are negative values and dark shadings with solid contours positive values), low-frequency wind speed $|\mathbf{u}_m|$ larger than 18 m s^{-1} (dotted shadings), negative values of the high-frequency geopotential (thick dashed contours, interval 250 m^2 s^{-2}) and dilatation axes: (a) 1800 UTC Day1, (b) 0000 UTC Day2, and (c) 0600 UTC Day2.

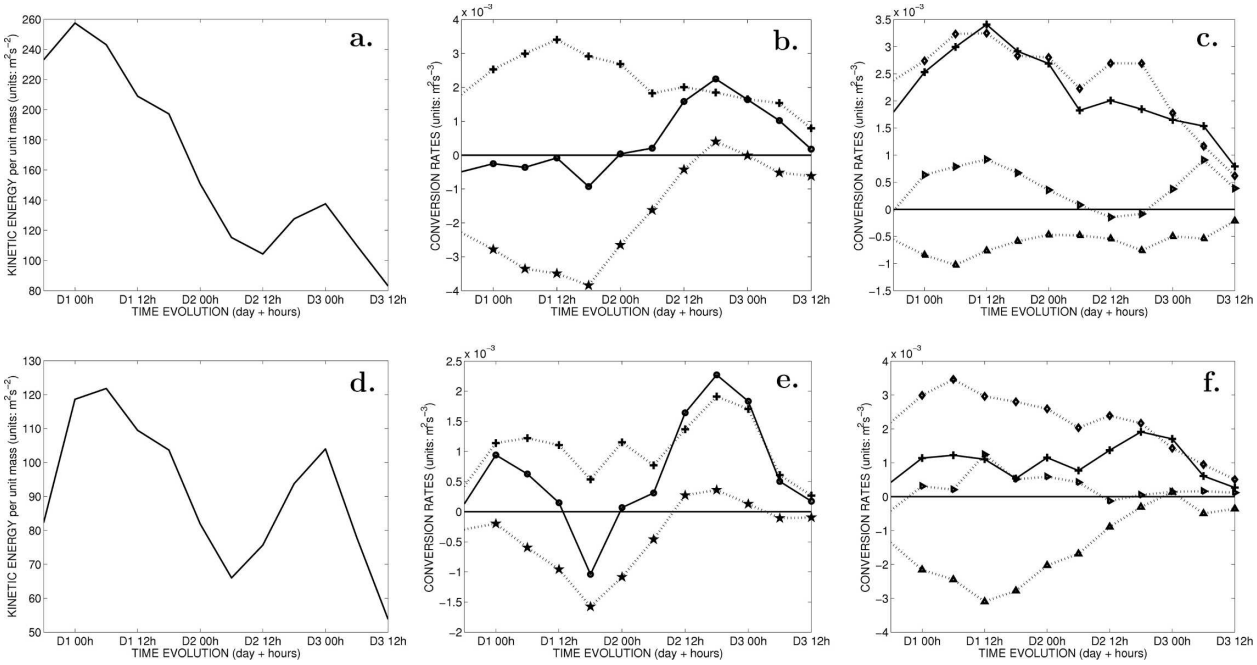

FIG. 10. Time evolution of volume integrals over IOP17 (a)–(c) between 200 and 900 hPa and (d)–(f) between 600 and 900 hPa; (a), (d) kinetic energy K_e' per unit mass (solid line, units: $m^2\,s^{-2}$); (b), (e) pressure work $-\mathbf{u}'\cdot\boldsymbol{\nabla}_p\Phi'$ (dotted line with + signs), Reynolds stress term $-\mathbf{u}'\cdot(\mathbf{u}_3'\cdot\boldsymbol{\nabla}_3\mathbf{u}_m)$ (dotted line with stars) and the sum of the two terms (solid line with circles); (c), (f) ageostrophic geopotential horizontal fluxes $-\boldsymbol{\nabla}_p\cdot(\mathbf{u}'\Phi')$ (dotted line with ▶ signs), vertical fluxes $-\partial(\omega'\Phi')/\partial p$ (dotted line with ▲ signs), baroclinic conversion rate $-\mathcal{R}\theta'\omega'$ (dotted line with diamonds), and total pressure work $-\mathbf{u}'\cdot\boldsymbol{\nabla}_p\Phi'$ (solid line with + signs).

sure work is the sum of three terms [see Eq. (11)] whose time evolutions are shown in Fig. 10.c. The baroclinic conversion term (Fig. 10c) is always positive, and has two maxima at 0600 UTC Day1 and at 1800 UTC Day2. The sign of the term related to the ageostrophic geopotential horizontal fluxes is anticorrelated with the kinetic energy variations. This anticorrelation is logical as this term is the dispersion term of kinetic energy; if kinetic energy increases, the term is negative around the region of increase and acts to redistribute energy away from this region; the opposite occurs if there is kinetic energy decrease. This term could be however important (see, e.g., Orlanski and Katzfey 1991) as it may redistribute energy from a growing cyclone to another one located downstream of it. But IOP17 is very far from any other active cyclones and cannot receive energy in that way. The ageostrophic geopotential vertical flux is always negative as it acts to disperse energy above the level 200 hPa and below 900 hPa. From Fig. 10c, we conclude that the positive sign of the pressure work is due to baroclinic conversion from eddy potential energy to eddy kinetic energy.

Similarly, consider Figs. 10d,e,f which are focused on the low-level cyclone. The K_e' curve (Fig. 10d) presents two peaks whose amplitudes are comparable to each other showing that the second deepening phase of the surface cyclone is as strong as the first one. The sign of the sum of the pressure work and the Reynolds stress (see Figs. 10e) is quite well correlated in time with the kinetic energy variations (Fig. 10d). The peak at 1800

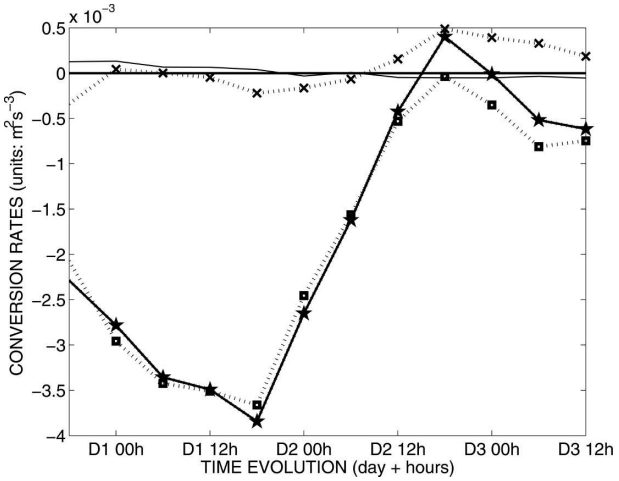

FIG. 11. Time evolution of the vertically averaged (200–900 hPa) barotropic generation rate $\mathbf{E}\cdot\mathbf{D}_m$ (dotted line with squares), divergence term $-K_e'(\boldsymbol{\nabla}_p\cdot\mathbf{u}_m)$ (thin solid line), vertical part of the Reynolds stress $-\omega'(\mathbf{u}'\cdot\partial\mathbf{u}_m/\partial p)$ (dotted line with crosses), and Reynolds stress term $-\mathbf{u}'\cdot(\mathbf{u}_3'\cdot\boldsymbol{\nabla}_3\mathbf{u}_m)$ (solid line with stars; growth rate units: $m^2\,s^{-3}$).

UTC Day2 of the sum of the two terms corresponds to both a peak of the Reynolds term and of the pressure work even though the positive sign is due essentially to the latter. The analysis of the pressure work in Fig. 10f first demonstrates, as in Fig. 10c, that the ageostrophic geopotential horizontal flux does not play a role in the peak of the pressure work and acts to disperse kinetic energy. However, a large difference has to be made between Fig. 10f and Fig. 10c with the ageostrophic geopotential vertical flux; this term has a large increase starting 1200 UTC Day1 and lasting for 36 h in Fig. 10f, which is not present in Fig. 10c. It means that a large part of the kinetic energy created in the upper levels is vertically redistributed downward in the low levels. This particular point on vertical redistribution of energy cannot be explained by invoking the theory described in sections 2 and 3 but it has to be taken into account to understand the particularly strong development of the surface cyclone. This term added to the significant positive baroclinic conversion rate is responsible for the peak of the pressure work at 1800 UTC Day2. The Reynolds stress term has a behavior similar to Fig. 10b, and is still dominated by the barotropic generation rate.

The energy budget analysis depicted in Fig. 10 supports the mechanism suggested above. The second growth stage is due to an interruption of the barotropic sink during the crossing of the jet and to significant positive baroclinic conversion rates; that is, to the maintenance of the baroclinic interaction between the upper disturbance and the surface cyclone far downstream of the baroclinicity maximum. Note that although the analysis of the conversion and redistribution energy terms does not allow the exact recovery of energy growth rates, as forcing, dissipation, and diabatic terms that may be important have been neglected, it is enough to explain the time variations of the IOP17 energy.

The different terms of Eq. (12) are now analyzed in Fig. 12 to investigate the nature of the baroclinic interaction. The baroclinic generation rate $T'_e|\mathbf{B}_c|$conf has essentially two local peaks, one at 0600 UTC Day1 (t_1), and the second at 1800 UTC Day2 (t_2) corresponding to the two growth stages of IOP17. Although the cyclone evolves in a baroclinicity $|\mathbf{B}_c|$ approximately 1.5 times larger at t_1 than at t_2 (see dash–dotted line), the term $|\mathbf{B}_c| \times$ conf (dashed line) is almost 1.5 times stronger at the second time than at the first one. It means that the configuration term during the second growth stage is more than twice larger than during the first one. Furthermore, the eddy total energy (dotted line) has diminished by a factor of 2 between the two dates. Finally, the baroclinic generation rate at t_2 is two-thirds (times) that at t_1 because of the decrease of both baroclinicity and total energy, but note it would be significantly weaker if there was no increase of the configuration term. Figure 12 underlines the large difference in dynamical processes of the two growth stages of IOP17; the first one occurs in large baroclinicity, whereas the second one is more characterized by the perturbation taking an optimal baroclinic configuration.

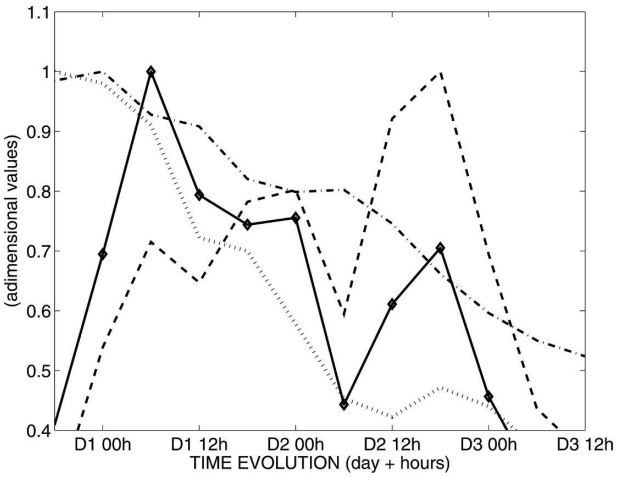

FIG. 12. Time evolution of volume integrals over IOP17 between 200 and 900 hPa of the baroclinic generation rate $T'_e|\mathbf{B}_c|$conf (thick solid line with diamonds), the low-frequency baroclinicity $|\mathbf{B}_c|$ (dash–dotted line), the high-frequency total energy T'_e per unit mass (dotted line), and $|\mathbf{B}_c|$conf (dashed line). Each variable is divided by its maximum during the period considered in order to compare its evolution to other variables.

Figure 13 exhibits the same idea but from a spatial point of view as the pattern associated with the baroclinic generation rate $T'_e|\mathbf{B}_c|$conf (Fig. 13a) bears a close resemblance at 1800 UTC Day2 with that of $|\mathbf{B_c}|$. conf (Fig. 13b) and not at all with that of the baroclinicity $|\mathbf{B}_c|$. The peak of the baroclinic generation rate is thus definitely due to the configuration term. It is interesting to note that the location of the baroclinic generation rate and most of its spatial pattern can be recovered from the quantity $|\mathbf{B_c}|$ conf, which it is not proportional to the high-frequency amplitude, as only the environmental baroclinicity and the configuration term intervene.

6. Discussion

A new diagnostic parameter, called effective deformation Δ_m, has been introduced in this study following the quasigeostrophic theory of RHK03 and RHK04. Our results indicate that it is relevant to analyze the role played by the horizontal inhomogeneities of the large-scale flow in locating and triggering the development of midlatitude cyclones. Regions in the upper tro-

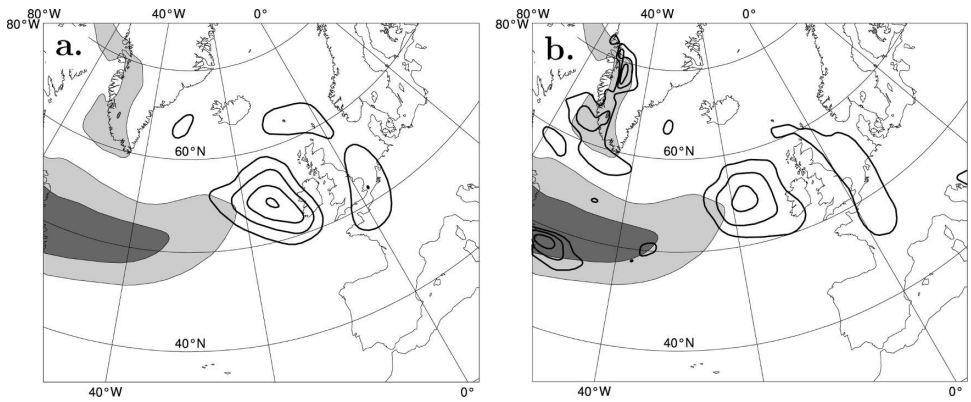

FIG. 13. Vertical average (900–200 hPa) at 1800 UTC Day2 of the low-frequency baroclinicity $|\mathbf{B}_c|$ larger than 3×10^{-5} s^{-1} (shaded contours, interval 10^{-5} s^{-1}) with (a) that of the baroclinic generation rate $T'_e|\mathbf{B}_c|$conf larger than 2 m^2 s^{-3} (thick solid contours, interval 2 m^2 s^{-3}) and (b) that of $|\mathbf{B}_c|$conf larger than 10^{-5} s^{-1} (thick solid contours, interval 5×10^{-6} s^{-1}).

posphere where the low-frequency criterion $\Delta_m > 0$ is satisfied; that is, where the low-frequency deformation magnitude is greater than the absolute value of the low-frequency vorticity are shown to coincide with the localization of the high-frequency disturbances at the same level. From the knowledge of this criterion, one is able to deduce at each longitude on which side of the jet (cyclonic or anticyclonic) synoptic eddies tend to be located. This new criterion highlights subtle differences between low frequencies zonal-like jet flows that the associated distributions of deformation or vorticity considered separately does not allow to detect. Yet, the path of eddies turns out to be different for several such flows, and the effective deformation allows for predicting this difference correctly.

More precisely, the horizontal maps determined by the criterion $\Delta_m > 0$ present distinct large-scale regions inside which the dilatation axes have almost the same orientation. When two such consecutive regions are located on both sides of the jet maximum, the transition from the first region to the next one reduces to a contact point accompanied by a sudden change of the dilatation axes orientation: this combined configuration defines a barotropic critical region. It is a specific place where barotropic development has very good chances to occur. Two of these barotropic critical regions have been demonstrated to be the preferred region where synoptic eddies tend to cross the jet from the south to the north. Two case studies detail this behavior: one is related to the upper-level precursor that leads to the storm Martin in December 1999 and the other to IOP17 of FASTEX. The scenario can be summarized as follows: during its travel on the anticyclonic side, the high-frequency eddy develops a strong south–west to north–east tilt, indicating a strong elongation along the dilatation axes and hence a large barotropic decrease but as it is crossing the barotropic critical region, the eddy is rapidly reshaped and goes through a stage of barotropic growth or at least there is an interruption of the barotropic sink.

The original idea for such a barotropic process comes from the theoretical study of Farrell (1989) and is the following; a perturbation embedded in a confluent flow will be stretched zonally and will be compacted in the diffluent flow region leading to perturbation kinetic energy growth. This barotropic process has been already proved to be important in real cases for the formation of disturbances in the upper troposphere (Lackmann et al. 1999; Kucharski and Thorpe 2000) but is shown here to take place at low levels as well as at upper levels and differs from a wave instability mechanism. Furthermore, our approach predicts from the large-scale flow alone the regions where such dynamics are likely to occur. It should be emphasized that such a critical region cannot be reduced to the mere separation between a confluence and a diffluence.

While these processes occur about any barotropic critical regions, they explain only a small part of cyclone developments. The way these interact with the more powerful baroclinic interaction depends on where the BtCR is located with respect to the jet exit. When both are collocated, such a constructive interaction has been identified: first, the constructive barotropic mechanism takes place as indicated above. This creates new amplitude farther downstream of the original system, and therefore increases its vertical tilt. This in turn enables a new burst of baroclinic growth, away from the maximum baroclinicity. Again, no instability needs to be called upon. The mechanism just described shows how barotropic processes can modify the baroclinic interac-

tion between a surface cyclone and an upper-level disturbance, it provides a rationale for the FASTEX cyclones strengthening during their crossing of the jet in the jet-exit region as described by Baehr et al. (1999) since they all occurred in a similar jet configuration. What happens when the jet exit is not collocated with a BtCR, as in December 1999, is the aim of Part II (Rivière and Joly 2006) of our study.

Acknowledgments. The authors thank Philippe Arbogast for his useful comments on this work as well as the suggestions of the three anonymous reviewers that have significantly helped to clarify the presentation of the manuscript. The advice of Lien Hua and Patrice Klein is also sincerely acknowledged. G. Rivière was supported by a postdoctoral fellowship from Ecole Doctorale de l'Ecole Polytechnique during this work.

APPENDIX

Density Function

In this appendix, the algorithm leading to the high-frequency relative vorticity density of Fig. 3 is described. The density function $D(x, y)$ is first initialized to zero. At each time step during the period of interest, and at each grid point (x_0, y_0) satisfying the threshold condition $\zeta' > 1.2 \times 10^{-4}$, we consider all its neighboring grid points (x, y) [those belonging to a circle centered in (x_0, y_0) whose diameter corresponds to 4° in latitude] satisfying also the threshold condition $\zeta' > 1.2 \times 10^{-4}$, and the density function for these particular grid points is incremented by one. Such a definition of the density function $D(x, y)$ gives a stronger weight to grid points surrounded by other ones satisfying also the threshold condition. It leads to smoother contours than if we had used the simple definition that consists to count the number of times during the period of interest that each grid point satisfies the threshold condition but does not change the results.

REFERENCES

Arbogast, P., 2004: Frontal wave development by interaction between a front and a cyclone: Application to the FASTEX IOP 17. *Quart. J. Roy. Meteor. Soc.,* **130,** 1675–1696.

Ayrault, F., 1998: Environnement, structure et évolution des dépressions météorologiques: Réalité climatologique et modèles types. Ph.D. thesis, Université P. Sabatier, Toulouse, France, 328 pp.

——, and Joly, A., 2000: Une nouvelle typologie des dépressions météorologiques: Classification des phases de maturation. *Compt. Rend. Acad. Sci. Paris, Earth Planet Sci.,* **330,** 167–172.

Baehr, C., B. Pouponneau, F. Ayrault, and A. Joly, 1999: Dynamical characterization of the FASTEX cyclogenesis cases. *Quart. J. Roy. Meteor. Soc.,* **125,** 3469–3494.

Barcilon, A., and C. H. Bishop, 1998: Nonmodal development of baroclinic waves undergoing horizontal shear deformation. *J. Atmos. Sci.,* **55,** 3583–3597.

Bishop, C. H., 1993: On the behavior of baroclinic waves undergoing horizontal deformation. I: The "RT" phase diagram. *Quart. J. Roy. Meteor. Soc.,* **119,** 221–240.

——, and A. J. Thorpe, 1994: Frontal wave stability during moist deformation cyclogenesis. II: The suppression of non-linear wave development. *J. Atmos. Sci.,* **51,** 874–888.

Black, R. X., and R. M. Dole, 2000: Storm tracks and barotropic deformation in climate models. *J. Climate,* **13,** 2712–2728.

Cai, M., and M. Mak, 1990: On the basic dynamics of regional cyclogenesis. *J. Atmos. Sci.,* **47,** 1417–1442.

Cammas, J. P., and Coauthors, 1999: FASTEX IOP17 cyclone: Introductory synoptic study with field data. *Quart. J. Roy. Meteor. Soc.,* **125,** 3393–3414.

Chaboureau, J. P., and A. J. Thorpe, 1999: Frontogenesis and the development of secondary wave cyclones in FASTEX. *Quart. J. Roy. Meteor. Soc.,* **125,** 925–940.

Davies, H. C., C. Schar, and H. Wernli, 1991: The palette of fronts and cyclones within a baroclinic wave-development. *J. Atmos. Sci.,* **48,** 1666–1689.

Desroziers, G., G. Hello, and J.-N. Thepaut, 2003: Four-dimensional reanalyses of FASTEX. *Quart. J. Roy. Meteor. Soc.,* **129,** 1301–1315.

Evans, M. S., D. Keyser, L. F. Bosart, and G. M. Lackmann, 1994: A satellite-derived classification scheme for rapid maritime cyclogenesis. *Mon. Wea. Rev.,* **122,** 1381–1416.

Farrell, B. F., 1989: Transient development in confluent and diffluent flow. *J. Atmos. Sci.,* **46,** 3279–3288.

Hoskins, B. J., and N. V. West, 1979: Baroclinic waves and frontogenesis. Part II: Uniform potential vorticity jet flows—Cold and warm fronts. *J. Atmos. Sci.,* **36,** 1663–1680.

James, I. N., 1987: Suppression of baroclinic instability in horizontally sheared flows. *J. Atmos. Sci.,* **44,** 3710–3720.

Joly, A., and Coauthors, 1999: Overview of the field phase of the Fronts and Atlantic Storm-Track Experiment (FASTEX) project. *Quart. J. Roy. Meteor. Soc.,* **125,** 3131–3163.

Koh, T.-Y., and B. Legras, 2002: Hyperbolic lines and the stratospheric polar vortex. *Chaos,* **12,** 382–394.

Kucharski, F., and A. J. Thorpe, 2000: Upper-level barotropic growth as a precursor to cyclogenesis during FASTEX. *Quart. J. Roy. Meteor. Soc.,* **126,** 3219–3232.

Lackmann, G. M., D. Keyser, and L. F. Bosart, 1999: Energetics of an intensifying jet streak during the experiment on rapidly intensifying cyclones over the Atlantic (ERICA). *Mon. Wea. Rev.,* **127,** 2777–2795.

Lapeyre, G., P. Klein, and B. L. Hua, 1999: Does the tracer gradient vector align with the strain eigenvectors in 2D turbulence. *Phys. Fluids A,* **11,** 3729–3737.

Lau, N.-C., 1988: Variability of the observed midlatitude storm tracks in relation to low-frequency changes in the circulation pattern. *J. Atmos. Sci.,* **45,** 2718–2743.

Lee, W.-J., and M. Mak, 1996: The role of orography in the dynamics of storm tracks. *J. Atmos. Sci.,* **53,** 1737–1750.

Mak, M., and M. Cai, 1989: Local barotropic instability. *J. Atmos. Sci.,* **46,** 3289–3311.

Mallet, I., P. Arbogast, C. Baehr, J. P. Cammas, and P. Mascart, 1999a: Effects of a low-level precursor and frontal stability on cyclogenesis during FASTEX IOP17. *Quart. J. Roy. Meteor. Soc.,* **125,** 3415–3437.

——, J. P. Cammas, P. Mascart, and P. Bechtold, 1999b: Effects of cloud diabatic heating on the early development of the FASTEX IOP17 cyclone. *Quart. J. Roy. Meteor. Soc.,* **125,** 3439–3467.

Orlanski, I., and J. Katzfey, 1991: The life cycle of a cyclone wave in the Southern Hemisphere. Part I: Eddy energy budget. *J. Atmos. Sci.,* **48,** 1972–1998.

——, and J. P. Sheldon, 1995: Stages in the energetics of baroclinic systems. *Tellus,* **47A,** 605–628.

Pierrehumbert, R. T., 1984: Local and global instability of zonally varying flow. *J. Atmos. Sci.,* **41,** 2141–2162.

Rivière, G., and A. Joly, 2006: Role of the low-frequency deformation field on the explosive growth of extratropical cyclones at the jet exit. Part II: Baroclinic critical region. *J. Atmos. Sci.,* **63,** 1982–1995.

——, B. L. Hua, and P. Klein, 2003: Perturbation growth in terms of barotropic alignment properties. *Quart. J. Roy. Meteor. Soc.,* **129,** 2613–2635.

——, ——, and ——, 2004: Perturbation growth in terms of baroclinic alignment properties. *Quart. J. Roy. Meteor. Soc.,* **130,** 1655–1673.

Sanders, F., 1993: Upper-level geostrophic diffluence and deepening of surface lows. *Wea. Forecasting,* **8,** 339–344.

Santurette, P., and A. Joly, 2002: ANASYG/PRESYG, Météo-France's new graphical summary of the synoptic situation. *Meteor. Appl.,* **9,** 129–154.

Schultz, D. M., D. Keyser, and L. F. Bosart, 1998: The effect of large-scale flow on low-level frontal structure and evolution in midlatitudes cyclones. *Mon. Wea. Rev.,* **126,** 1767–1791.

Shutts, G. J., 1983: The propagation of eddies in diffluent jet streams: Eddy vorticity forcing of "blocking" flow fields. *Quart. J. Roy. Meteor. Soc.,* **109,** 737–761.

Sickmoller, M., R. Blender, and K. Fraedrich, 2000: Observed winter cyclone tracks in the Northern Hemisphere in re-analysed ECMWF data. *Quart. J. Roy. Meteor. Soc.,* **126,** 591–620.

Simmons, A. J., and B. J. Hoskins, 1980: Barotropic influences on the growth and decay of baroclinic waves. *J. Atmos. Sci.,* **37,** 1679–1684.

Thorncroft, C. D., B. J. Hoskins, and M. E. McIntyre, 1993: Two paradigms of baroclinic-wave life-cycle behavior. *Quart. J. Roy. Meteor. Soc.,* **119,** 17–55.

Uccellini, L. W., 1990: Processes contributing to the rapid development of extratropical cyclones. *Extratropical Cyclones: The Erik Palmen Memorial Volume,* C. Newton and E. O. Holopainen, Eds., Amer. Meteor. Soc., 81–105.

Vautard, R., 1990: Multiple weather regimes over the North Atlantic: Analysis of precursors and successors. *Mon. Wea. Rev.,* **118,** 2056–2081.

Whitaker, J. S., and A. Barcilon, 1992: Type B cyclogenesis in a zonally varying flow. *J. Atmos. Sci.,* **49,** 1877–1892.

Young, M. V., 1995: Types of cyclogenesis. *Images in Weather Forecasting,* M. J. Bader et al., Eds., Cambridge University Press, 213–286.